

Nanoparticle Immobilization for Controllable Experiments in Liquid-Cell Transmission Electron Microscopy

Alex W. Robertson,^{1,2†}, Guomin Zhu^{1†}, B. Layla Mehdi^{1,3}, Robert M. J. Jacobs,⁴ James De Yoreo¹, Nigel
D. Browning^{1,3}*

¹Physical & Computational Science Directorate, Pacific Northwest National Laboratory, Richland, WA
99352 United States

²Department of Materials, University of Oxford, Parks Road, Oxford, OX1 3PH, United Kingdom

³School of Engineering, University of Liverpool, Liverpool, L69 3GH, United Kingdom

⁴Department of Chemistry, Chemistry Research Laboratory, University of Oxford, Mansfield Road,
Oxford OX1 3TA, United Kingdom

*alex.w.robertson@gmail.com; †Contributed equally.

KEYWORD: liquid-cell TEM, in-situ TEM, nanoparticle, nucleation, silanization

ABSTRACT

We demonstrate that silanization can control the adhesion of nanostructures to the SiN windows compatible with liquid-cell transmission electron microscopy (LC-TEM). Formation of an APTES self-assembled monolayer on a SiN window, producing a surface decorated with amino groups, permits strong adhesion of Au nanoparticles to the window. Many of these nanoparticles remain static, undergoing minimal translation or rotation during LC-TEM up to high electron beam current densities due to the strong interaction between the APTES amino group and Au. We then use this technique to

perform a direct comparative LC-TEM study on the behavior of ligand and non-ligand coated Au nanoparticles in a Au growth solution. While the ligand coated nanoparticles remain consistent even under high electron beam current densities, the naked nanoparticles acted as sites for secondary Au nucleation. These nucleated particles decorated the parent nanoparticle surface, forming consecutive monolayer assemblies of ~2 nm diameter nanoparticles, which sinter into the parent particle when the electron beam was shut off. This method for facile immobilization of nanostructures for LC-TEM study will permit more sophisticated and controlled in-situ experiments into the properties of solid-liquid interfaces in the future.

Introduction

The chemical engineering of nanoparticles and associated nanostructures has proven invaluable in the development of more efficient catalysts. Fundamental chemical processes that constitute the core of many emerging green technologies, such as the oxygen reduction reaction in hydrogen fuel cells,¹⁻⁴ and the hydrodeoxygenation reaction for biofuel processing,⁵ can enjoy vastly improved efficiencies courtesy of the exploitation of rationally designed nano-catalysts. The informed development of these catalyst nanostructures necessitates an accurate understanding of the catalyst shape, with active site exhibition, prevalence, and resilience all valuable information to be fed into improvement of the catalyst synthesis procedure. Transmission electron microscopy (TEM) has proven to be an essential tool for achieving this, and with the emergence and continued development of liquid-cell (LC-) TEM there has been an increased understanding of the fundamental processes that occur during nanoparticle growth and subsequent chemical reactions.⁶⁻¹¹

While a powerful technique, LC-TEM has several limitations and difficulties, with resolution reduction and beam damage foremost among them.^{12,13} Preventing the unwanted motion of nanostructures, for instance to allow for more detailed studies of their structural evolution without having to worry about tracking, can be difficult. Fortunately, diffusion rates inside the thin liquid-cells employed in LC-TEM are many orders of magnitude lower than that of bulk liquids,¹⁴⁻¹⁶ and can in some cases even be useful;¹⁷ however sample motion can still prevent detailed temporal studies, in particular where high magnifications and thus small fields of view are desired. The ability to anchor pre-

prepared nanostructures on the liquid-cell membranes prior to assembly of the liquid-cell would prevent this unwanted motion. This would have the additional advantage of permitting more reliable ex-situ characterization of the same sample before and after the in-situ experiment, as the nanostructures would be consistently fixed to the membrane.

Adhesion of a nanostructure to a membrane could conceivably employ one of several fundamental routes; the van der Waals interaction, electrostatic charging, mechanical interlocking, or chemical bonding.¹⁸ Mechanical interlocking, where an adhesive permeates into any surface irregularities to permit fixing, can be eliminated for LC-TEM due to the smoothness of the silicon nitride membranes. Employing the electrostatic force by prior charging of the membrane window and nanostructures, as used for adhering toner to paper in a printer, would be undermined by the charging effect of the TEM beam during experiments. Van der Waals and electrostatic forces are the interaction forces that dominate between nanostructures and the membrane window under standard LC-TEM conditions regardless, yielding the observed ‘stop-start’ motion of nanoparticles,¹⁶ thus improving nanostructure fixing would require something further. By process of elimination chemical bonding is the remaining option.

Silanization, where silane compounds are reacted with a substrate in order to decorate it with a self-assembled monolayer (SAM) of organic functional groups, is frequently used in biology to control the adhesion of proteins and other bio-molecules to surfaces.^{19,20} In particular APTES – (3-aminopropyl) triethoxysilane – is commonly employed due to its amino group termination, thus silanization with APTES yields a substrate decorated with outward facing amino groups that can strongly interact with many relevant molecules. In the context of inorganic chemistry, silanization with APTES has also been shown to enhance adhesion of Au nanoparticles to surfaces due to the strong interaction with the capping ligands.^{21–23}

Here, we demonstrate a silanization technique to immobilize Au nanoparticles for controlled LC-TEM characterization. Silanization with APTES results in the fixing of a significant proportion of the Au nanoparticle population, with many nanoparticles remaining adhered independently of TEM beam dose. We then demonstrate the techniques use by directly comparing the nucleation and growth of ligand decorated and non-decorated Au nanoparticles.

Results and Discussion

Several APTES silanization recipes suitable for functionalization of a silicon nitride substrate were explored, with the most effective determined by monitoring the yield with which drop-cast citrate-stabilized Au nanoparticles adhered to the substrate versus a non-treated control. Ex-situ STEM imaging was employed to demonstrate that 5 nm diameter Au nanoparticles stuck to the optimally treated SiN substrate over $100\times$ more effectively than for the non-treated case (Supporting Figure S1). For this recipe, the SiN substrates were first hydrolyzed by five minute oxygen plasma etch (power 10.5 W). This prepared the SiN surface with hydroxyl groups suitable for attack by APTES.²⁴ The substrates were then immediately immersed in 3% APTES solution for 60 minutes at 75 °C, forming a SAM on the SiN, and subsequently rinsed in ethanol for 15 minutes, rinsed in DI water, and blow dried. Citrate-stabilized Au nanoparticles were then applied by drop-casting and left to dry overnight prior to liquid-cell assembly.

These pre-loaded SiN windows were mounted into the liquid-cell holder along with an opposing blank SiN window and DI water. The mobility of the pre-loaded, APTES-SAM immobilized nanoparticles was compared to an Au nanoparticle solution between two non-treated SiN windows (Figure 1a-d). The imaged nanoparticles interacted with the SiN window, however they were observed to move freely under the electron beam, as indicated by the yellow arrows, and could detach from the window. In contrast, Au nanoparticles on the APTES treated window (Figure 1e-h) were observed to remain fixed over prolonged imaging at beam current densities (BCD) of $5.9 \times 10^3 \text{ e nm}^{-2} \text{ s}^{-1}$.

It is known that electron irradiation of water can lead to the formation of bubbles in the liquid-cell,²⁵ effectively reducing the water thickness to a thin (~ 40 nm) layer between the window and the bubble.²⁶ In previous LC-TEM studies, nanoparticles in this thin layer have been observed to be significantly more mobile; Supporting Movie S1 shows LC-STEM of the edge of a bubble, illustrating the relative mobility of nanoparticles in the thin- and thick-water regions. Supporting Movie S2 shows a high magnification LC-TEM view of these highly mobile thin-water layer dynamics. Care was taken to avoid comparing to nanoparticle mobility under a bubble, with the data presented in Figure 1a-d imaged in a region with no bubble formation observed (BCD of $5.9 \times 10^3 \text{ e nm}^{-2} \text{ s}^{-1}$). Data showing the typical nanoparticle motion

from a thin water region beneath a bubble is presented in Supporting Figure S2. Interestingly, we did not encounter bubble formation across any of our LC-TEM experiments performed with the silanized SiN windows, under dose rates ranging from 10^2 to $10^4 \text{ e nm}^{-2} \text{ s}^{-1}$. The different surface composition might preclude the formation of nanobubbles due to unfavorable energetics, however the moderate hydrophobicity of the APTES-SAM surface would be expected to encourage rather than inhibit bubble formation.²⁷ Alternatively, it is possible that the organic layer acts as a sink for the products formed from the radiolysis of water, precluding gas accumulation.

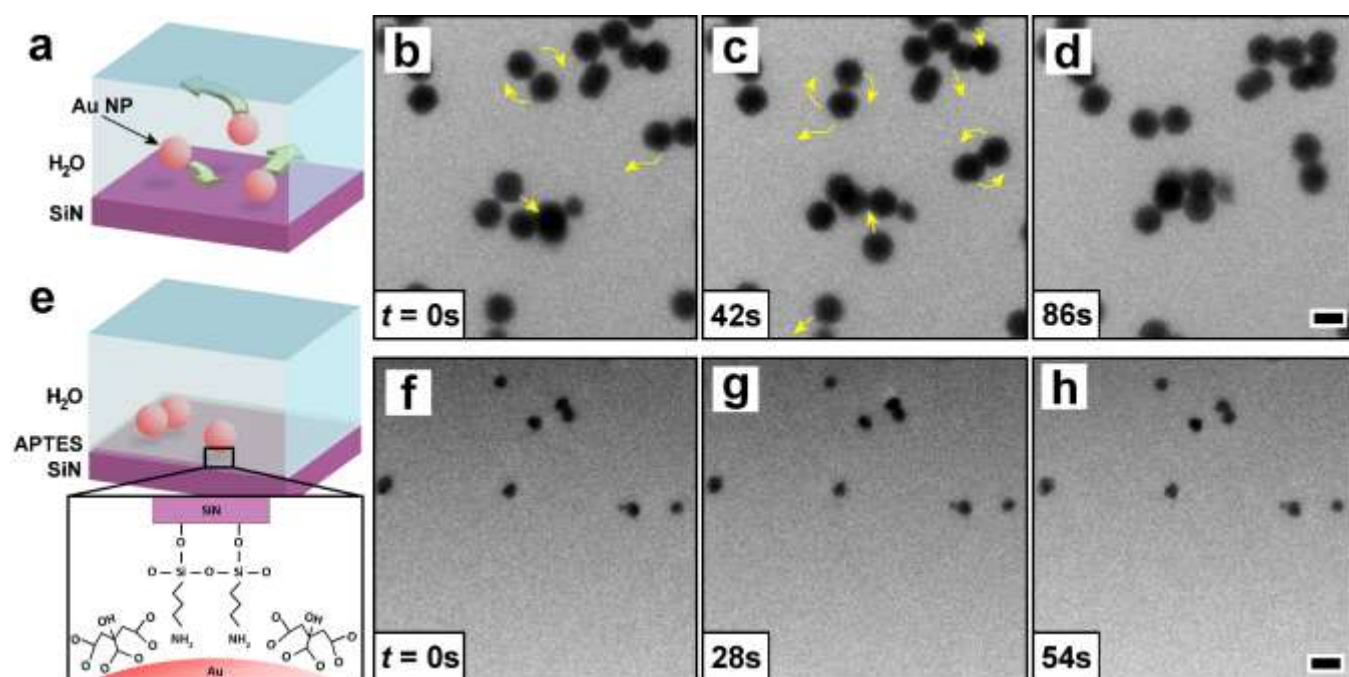


Figure 1. (a) Schematic of a standard liquid cell containing Au nanoparticles in water. (b-d) LC-TEM of mobile Au nanoparticles ($\sim 40 \text{ nm}$ diameter) contained between non-treated silicon nitride windows. (e) Schematic of a liquid cell with an APTES-SAM coating a SiN membrane window. The amino groups strongly interact with the Au nanoparticles, immobilizing them on the SiN. (f-h) LC-TEM of static Au nanoparticles ($\sim 25 \text{ nm}$ diameter), fixed by APTES functionalization to the SiN. Scale bars are 50 nm . BCD $5.9 \times 10^3 \text{ e nm}^{-2} \text{ s}^{-1}$.

The Au nanoparticles affixed to the APTES coated windows were observed to maintain their rotation as well as their position, as shown by the LC-TEM time-series in Figure 2a-d. Imaging under higher BCD ($9.4 \times 10^3 \text{ e nm}^{-2} \text{ s}^{-1}$) led to the movement of some of the nanoparticles affixed to the APTES, as indicated by red arrows in the LC-TEM time-series presented in Figure 2a-d. This effect will be discussed later. For the nanoparticles that remained fixed in their positions (colored boxes in Figure 2a-d), it was observed that they maintained their absolute orientation as well (Figure 2e-i), which we

attribute to the effect of the coated window. This is evident from detailed inspection of their faceting arrangement, which suggests they underwent minimal rotation under the electron beam; a change in faceting is observable between frame Figure 2h and i, as indicated by the annotation, and a slight rotation of the bottom particle across the four frames can also be discerned. The ability to prevent the rotation of nanoparticles under the electron beam in LC-TEM experiments will have value for the tracking of facet dependent reactions and growth, as the same facet might be tracked over the course of a reaction.

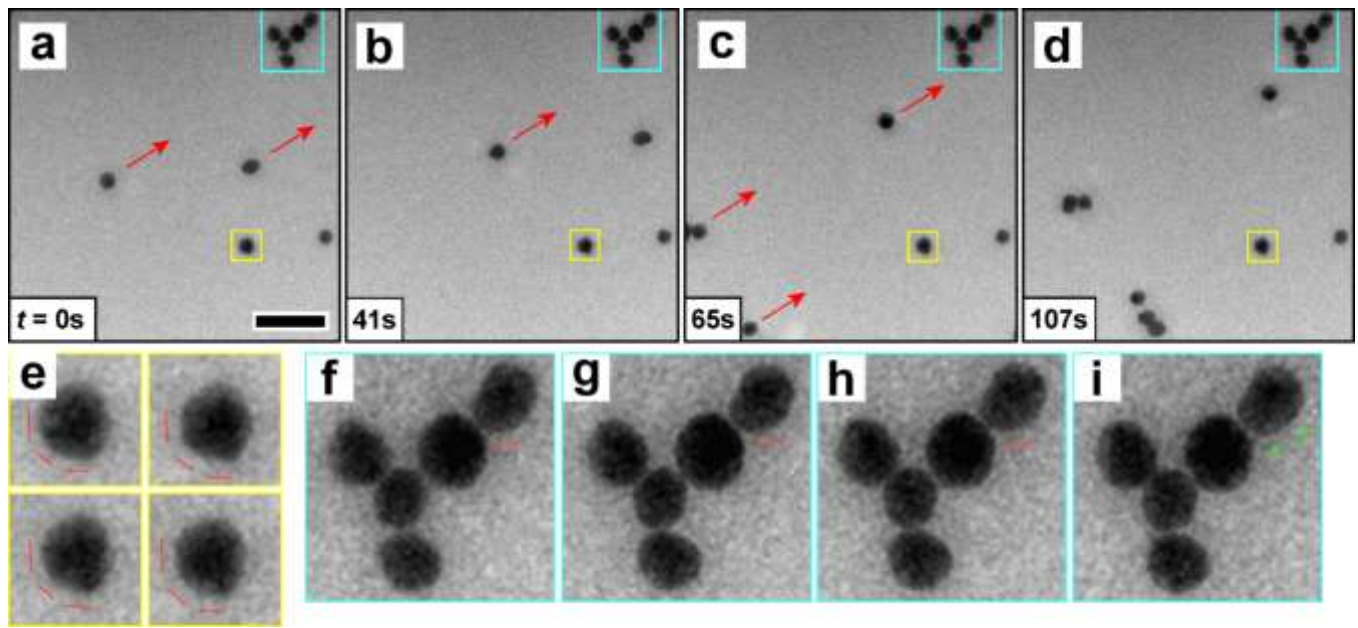


Figure 2. (a-d) LC-TEM time series of Au nanoparticles on the APTES functionalized membrane. Boxed particles remain fixed, red arrows indicate the constant motion of the mobile particles. Scale bar 50 nm. (e) Magnified view of the yellow boxed nanoparticle, with red lines indicating the constant exhibition of similar facets, suggesting a lack of particle rotation. (f-i) Magnified view of the cyan boxed nanoparticles, which largely maintain their relative configuration and faceting. The green line annotation in (i) indicates a change in facet exhibition from that indicated by the red lines in (f-h). BCD $9.4 \times 10^3 \text{ e nm}^{-2} \text{ s}^{-1}$.

As seen in Figure 2, the effect of higher BCD led to the uniform displacement of some of the Au nanoparticles across the SiN window. Figure 3a-c shows an LC-TEM time-series (Supporting Movie S3), with the BCD increased from 5.9×10^3 to $1.2 \times 10^4 \text{ e nm}^{-2} \text{ s}^{-1}$ at Figure 3b. No change in the position of the nanoparticles was observed in the initial 19 s (Figure 3a to b), however following the BCD increase movement of the nanoparticles highlighted in red was observed. These nanoparticles followed the track of the red arrows shown in Figure 3c, while the nanoparticles indicated with yellow

arrows remained static. Increasing the BCD further resulted in a concomitant increase in the particle speed, which was reversed upon BCD reduction, as shown in the time-series (Figure 3e-l, Supporting Movie S4) and plot (Figure 3m). The mobile nanoparticles maintained their relative position to one another, and moved at uniform speeds.

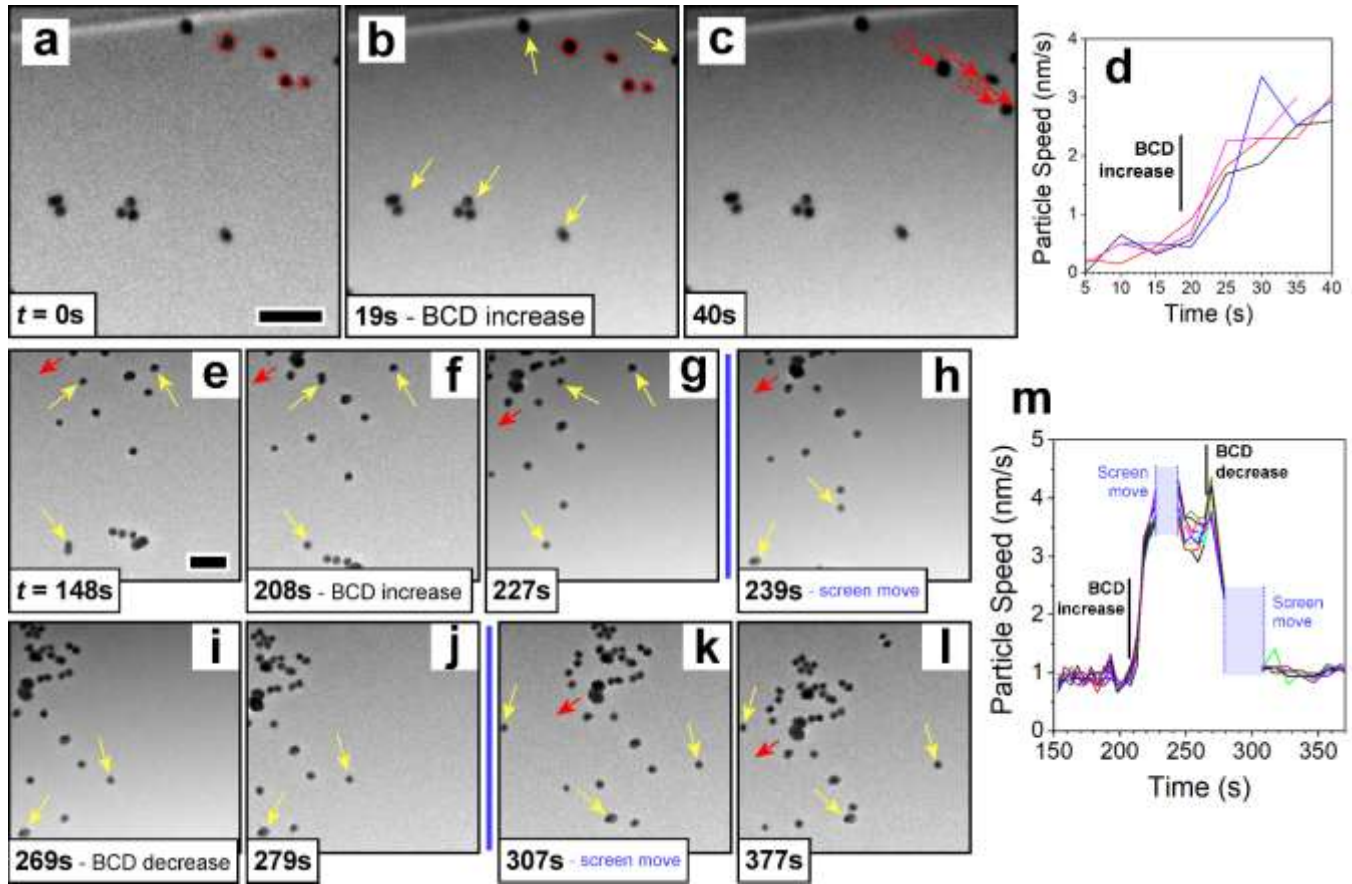


Figure 3. (a-c) LC-TEM time series demonstrating the effect of increasing BCD on nanoparticle immobility. Yellow arrows indicate nanoparticles that remain fixed, red highlight plus arrows indicate nanoparticles that move and their trajectory. The window edge along the top is a fixed reference. BCD increased from $5.9 \times 10^3 \text{ e nm}^{-2} \text{ s}^{-1}$ to $1.2 \times 10^4 \text{ e nm}^{-2} \text{ s}^{-1}$. (d) Measured speeds of the red highlighted nanoparticles in a-c. (e-l) LC-TEM time series illustrating the effect of BCD on nanoparticle speed. (m) Measured speeds of mobile nanoparticles in e-l. Scale bars are 100 nm. BCD increased from $5.9 \times 10^3 \text{ e nm}^{-2} \text{ s}^{-1}$ to $1.3 \times 10^4 \text{ e nm}^{-2} \text{ s}^{-1}$ and decreased back to $6.0 \times 10^3 \text{ e nm}^{-2} \text{ s}^{-1}$.

Condensing the electron beam ($\text{BCD} \sim 1 \times 10^4 \text{ e nm}^{-2} \text{ s}^{-1}$) yields a more pronounced Gaussian distribution to the beam intensity within the field of view, which led to scattering of the non-anchored nanoparticles in radial directions (Supporting Figures S3a-c), with observation of faster moving nanoparticles nearer the beam center (Supporting Figure S3d). Under the highest BCDs

$(2.0 \times 10^4 \text{ e nm}^{-2} \text{ s}^{-1})$ the mobile nanoparticles moved rapidly away from the beam center, although some still remain fixed to the SiN membrane (Supporting Figure S4).

The movement of nanoparticles at higher BCD is to be expected, as is their displacement from the irradiated region. Supporting Movie S5 shows similar nanoparticle behavior in a LC-STEM for a non-silanized liquid-cell. However, the behavior of the nanoparticles for our silanized samples showed differences; in Figure 2a-d and Figure 3 the mobile nanoparticles maintain their relative configuration with respect to one another, moving in synchronization, yet a significant number of other nanoparticles remain fixed even under high BCDs. While the behavior of the fixed nanoparticles is as we expect for citrate-capped Au nanoparticles strongly interacting with the SAM of APTES amino groups, the mechanism behind the unusual synchronized movement of multiple mobile nanoparticles is unexpected. We suggest that this movement is due to excess unreacted APTES forming an incomplete layer on top of the self-assembled APTES monolayer. Removal of the unreacted excess is difficult due to the mechanically delicate thin SiN windows precluding the use of more thorough rinsing techniques after silanization, such as ultrasonication in solvent, so excess APTES is likely despite the ethanol rinse. As this excess APTES is not anchored to the SiN substrate or interlinked into the SAM, it is more prone to displacement by the electron beam (Supporting Figure S5, Supporting Movie S6); the dose rate is sufficient to cause rapid damage to organic material (damage threshold for many organics $\sim 10^2$ to 10^3 e nm^{-2}),²⁸ and potentially also high enough to establish a temperature gradient. The displacement of this excess organic by the beam would also push along any Au nanoparticles that had not formed a strong interaction with the underlying APTES monolayer. The observation of many nanoparticles remaining static under irradiation suggests that these are successfully interacting with the base APTES monolayer, and that this base APTES monolayer remains in some form despite the relatively high electron dose rate.

Evidence supporting the excess organic layer model for the synchronized particle motion was revealed by capturing the interaction between mobile and fixed nanoparticles as they passed each other. Figure 4a-d show a LC-TEM time-series of some mobile nanoparticles moving past a fixed nanoparticle (yellow highlight). The fixed nanoparticle remains in the same position, and neither particle appears to

undergo any rotation or deviation during the overlap, suggesting that the mobile particle moves over the top of the fixed particle without collision. The lack of appreciable defocus differences for either set of nanoparticles would tend to rule out them being on opposite windows. We suggest that this observation is an effect of the unreacted APTES discussed above. If this unreacted layer is thicker than the Au nanoparticle diameter (Figure 4e), any nanoparticles on top of this layer would move over those that are bound by the APTES-SAM. In a separate observation, Figure 4f-k, a mobile nanoparticle is observed rotating as it displaces across a fixed particle, thus presumably colliding. We suggest the moving nanoparticle is residing on a sufficiently thin excess organic layer, thinner than the Au nanoparticle diameter, and so interacts with the fixed nanoparticle beneath (Figure 4l).

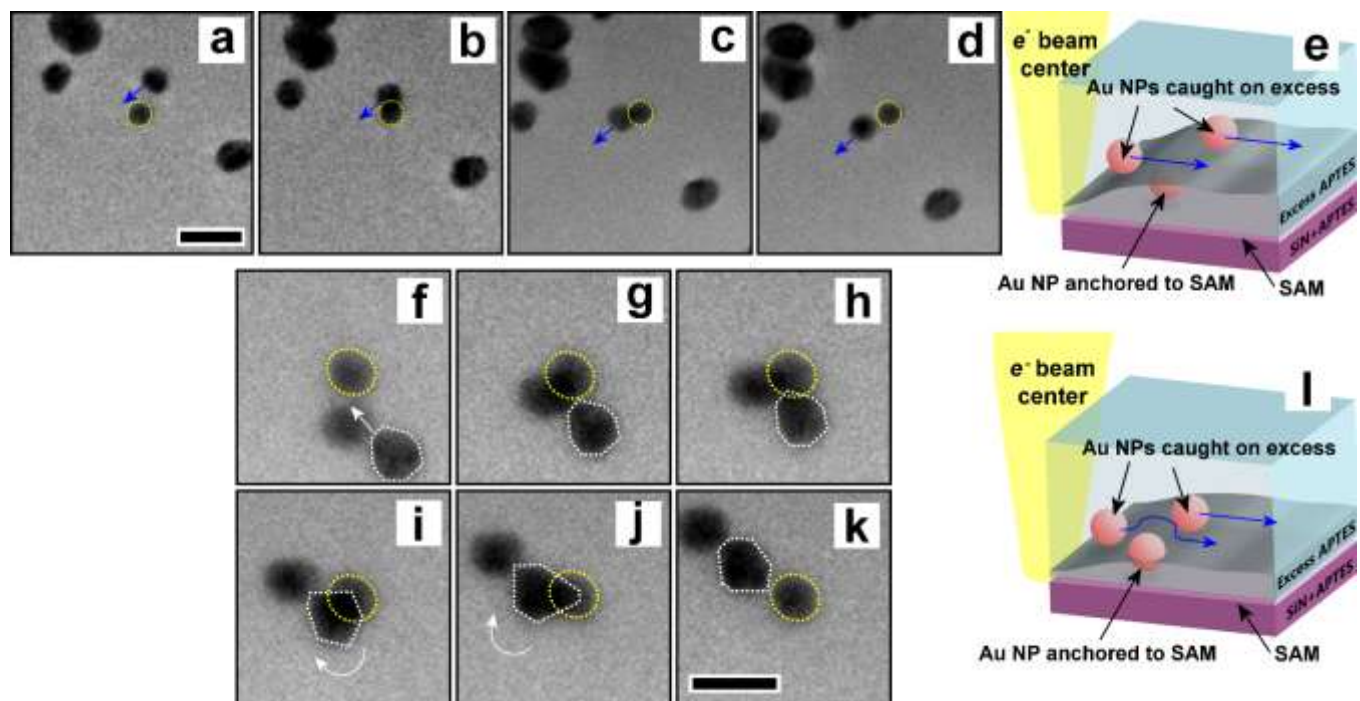


Figure 4. (a-d) LC-TEM image series showing a nanoparticle passing across an immobilized nanoparticle (yellow), with the fixed particle not being displaced. $BCD = 5.4 \times 10^3 \text{ e cm}^{-2} \text{ s}^{-1}$. (e) Schematic illustrating a mechanism for a-d, see main text for discussion. (f-k) LC-TEM image series showing a pair of nanoparticles moving past an immobilized nanoparticle (yellow). The faceting of the nanoparticle annotated in white was observed to change, suggesting its rotation. The immobilized nanoparticle remains fixed in place. $BCD = 1.4 \times 10^4 \text{ e cm}^{-2} \text{ s}^{-1}$ (l) Schematic of the mechanism causing the observation in f-k, see main text for discussion. Scale bars are 50 nm.

We performed a prototypical experiment utilizing the APTES immobilized citrate-capped Au nanoparticles by adding $2 \times 10^{-4} \text{ M}$ HAuCl_4 to the liquid-cell solution during assembly, allowing us to

directly contrast the behavior of the pre-deposited ligand passivated nanoparticles with newly nucleated particles with no ligand passivation. Under electron beam irradiation the Au precursor reduces, rapidly nucleating and growing Au nanoparticles between 20-50 nm diameter on the APTES functionalized surface (Supporting Figure S6).²⁹ While these initially nucleated nanoparticles are similar in size to those pre-deposited, there is a notable difference in their mobility. These newly nucleated nanoparticles rapidly move under the electron beam, forming into small linear clusters that settle on the membrane window (Supporting Figure S7, Supporting Movie S7),³⁰ confirming that the APTES-Au interaction is mediated by the citrate capping ligands. In Figure 5a and b a time-series illustrate the difference in behavior, with the top (blue) showing a rapidly moving aggregate of four newly nucleated nanoparticles, which settled into a fixed position after 70 s ($\text{BCD } 6.8 \times 10^2 \text{ e nm}^{-2} \text{ s}^{-1}$). The bottom (yellow) collection of five nanoparticles remained completely static through the same time. This suggests that the fixing of nanostructures to the surface amino groups is best performed prior to the experiment, rather than by nucleating these structures in-situ. As can be seen in the continuing time-series (Figure 5c-h), the nanoparticles do eventually separate, apparently instigated by the nucleation of new particles in between the initial nanoparticles (Figure 5d, white arrows), again suggesting a weaker bonding to the silanized surface.

The newly nucleated nanoparticles, lacking surface passivating ligand groups, continued to grow under the reducing action of the electron beam. These parent particles acted as sites for secondary nucleation events (Figure 5c-h). Over the course of the ~ 2200 s of imaging ($\text{BCD } 4.6 \times 10^3 \text{ e nm}^{-2} \text{ s}^{-1}$) nanoparticles and more amorphous Au structures were observed to precipitate out of the solution adjacent to the original four Au nanoparticles. At three stages during the observation the beam was blanked for a brief period, as indicated in Figure 5i, removing the reducing action of the electron beam. Observation immediately after the beam blanking revealed that on all occasions the newly formed Au structures had disappeared, having sintered into the adjacent parent Au nanoparticles (Supporting Figure S8). This is tracked in Figure 5i, which displays the increase in cross-sectional area of the initial four Au nanoparticles and the total area of the image consisting of precipitated Au.

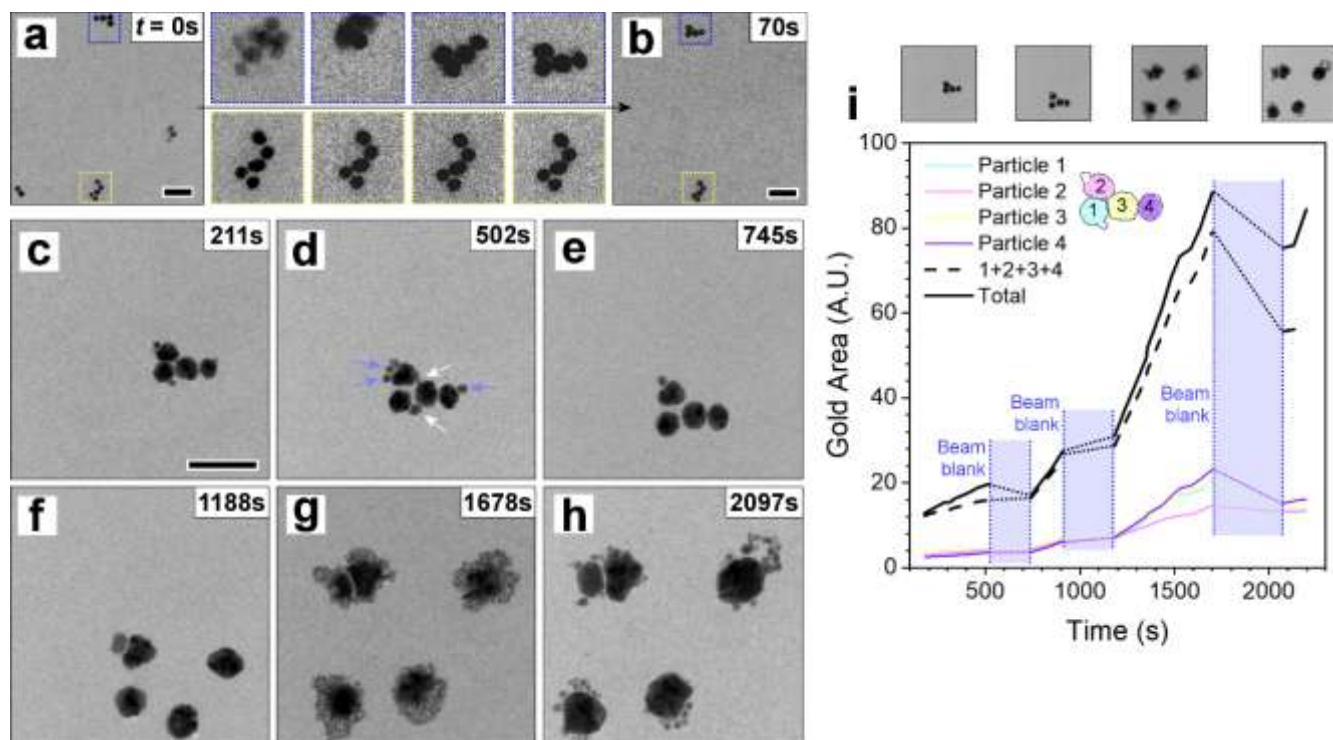


Figure 5. (a,b) Comparison of the motion exhibited by newly nucleated Au nanoparticles (top insert, blue) and pre-deposited, amino-fixed nanoparticles (bottom insert, yellow) over 70 s. BCD $6.8 \times 10^2 e \text{ nm}^{-2} \text{ s}^{-1}$. (c-h) Time-series following from (b) of the top nanoparticle group. Nanoparticles indicated by white and blue arrows vanish between (e) and (f) during beam blanking, sintering into the adjacent parent nanoparticles. White arrows indicate nanoparticles that form and push apart the established particles. BCD $4.6 \times 10^3 e \text{ nm}^{-2} \text{ s}^{-1}$. Scale bars 100 nm. (i) Change in nanoparticle cross-sectional area, both individually and in sum, plus the total gold present (i.e., from newly nucleated structures). The nanoparticle sizes leading up to the third beam blank are an overestimate, due to the difficulty in delineating the particle perimeter from the surrounding dense growths.

Similarly, under higher dose rates (BCD $3.7 \times 10^4 e \text{ nm}^{-2} \text{ s}^{-1}$) we observed the newly nucleated nanoparticles moved rapidly under the electron beam, while the pre-deposited nanoparticles remained well fixed to the silanized window (Figure 6). The pre-deposited nanoparticles do not move, nor do they act as sites for further Au nucleation from the solution. By contrast the larger nucleated nanoparticles, under the higher BCD, act as preferential nucleation sites for the rapid accumulation of ~ 2 nm diameter Au nanoparticles. As the insert in Figure 6b shows, these initially form as a monolayer adjacent to the parent particle, with extra consecutive layers forming on top. By Figure 6f these new nanoparticle-assemblies are entangled with the nearby pre-anchored nanoparticles. Shutting off the electron beam between Figure 6f and g lead to the dissolution/sintering of the freshly nucleated small nanoparticles

close to the parent nanoparticle, as in Figure 5, however the newly nucleated particles that were entwined with the anchored nanoparticles remain.

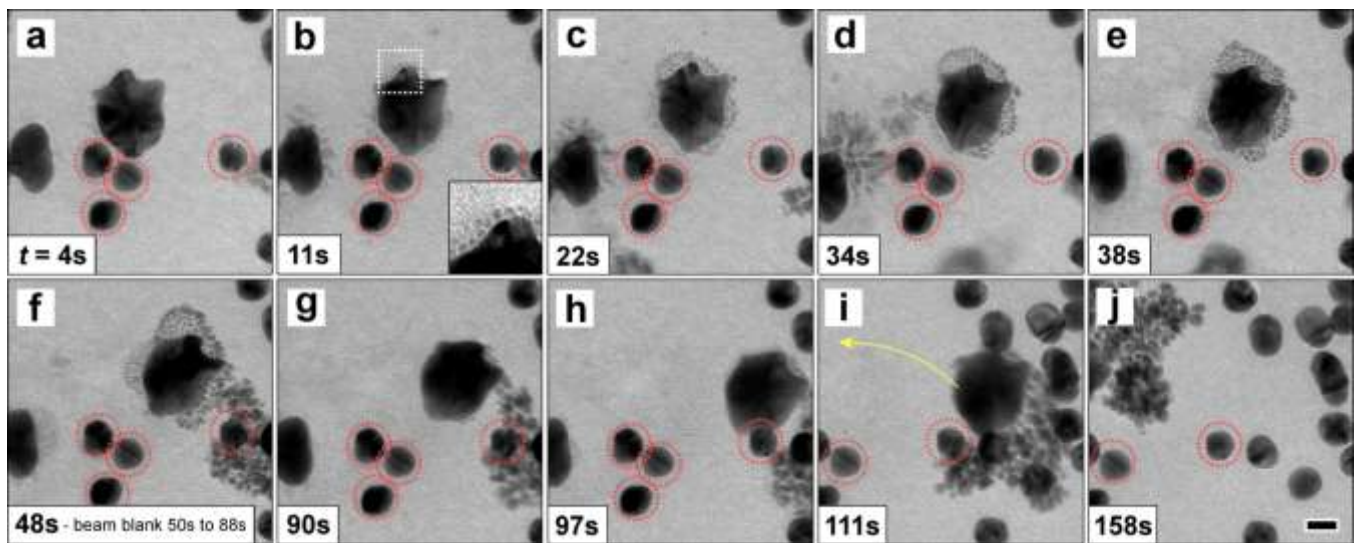


Figure 6. (a-j) LC-TEM time-series under high BCD, showing a larger newly nucleated and sintered nanoparticle moving rapidly while surrounding pre-deposited nanoparticles (red circles) remain fixed. The screen is moved between (h) and (i). Magnified insert to (b); small nanoparticles rapidly nucleated adjacent to the large new nanoparticle. Beam current density $3.7 \times 10^4 \text{ e nm}^{-2} \text{ s}^{-1}$. Scale bar 20 nm.

Conclusion

We present a simple method for the reliable adherence of nanostructures on to the SiN membrane windows employed in LC-TEM. Silanization of the SiN surface with APTES was particularly suitable for adhering Au nanostructures, which remain stably anchored for relevant electron beam current densities during LC-TEM. We utilized these pre-prepared silanized and Au nanoparticle decorated SiN windows to directly compare the difference in behavior of ligand passivated Au nanoparticles to freshly nucleated, non-passivated structures. The pre-deposited ligand coated Au nanoparticles remained effectively inert to the presence of Au precursor under the reducing action of the electron beam, however new Au nanoparticles nucleated from this acted in turn as nucleation sites for further nucleation of Au nanoparticles. These new particles decorated the parent particle surfaces, forming assembled monolayers while the electron beam was present, and sintering into the parent during beam blanking. The ability to adhere nanostructures to the SiN window, as presented here, will permit the design of more sophisticated and controllable liquid-cell experiments; such as those aimed at understanding the facet and growth

development of individual nanostructures, to advance nanostructure engineering; and tracking the dynamics of particle interactions under high pH/salt concentrations and the resulting emergent phenomena at larger scales, which is information that can inform models used to describe the complex chemical environment in radioactive waste.³¹

Methods

Sample Preparation

Au nanoparticles of between 20 and 50 nm diameter were synthesized by boiling a freshly prepared 50 ml HAuCl₄ solution (0.01% by weight), then adding 0.5 to 1.0 ml sodium citrate solution (1% by weight).³² Au nanoparticle seeds (3-5 nm diameter) were grown by preparing a 20 ml HAuCl₄ (2.5×10^{-4} M) and sodium citrate (2.5×10^{-4} M) solution, followed by the rapid addition of 0.6 ml ice-cold NaBH₄ (0.1 M) solution while stirring.³³

Several methods for silanization of the 30 nm thick SiN liquid-cell membranes were attempted, as discussed in the Supporting Information. The results presented in the main text used the following recipe: A 3% by volume solution of APTES in water was prepared and heated to 75 °C. SiN windows were cleaned and activated/hydrolyzed by oxygen plasma etching for 5 min at 10.5 W, before immediately being immersed in the prepared APTES solution and left for one hour. Membranes were removed and immersed in ethanol for 15 min, then rinsed in DI water and blow dried with nitrogen.

TEM Imaging and Analysis

LC-TEM was performed with an aberration corrected objective FEI Titan at 300 kV and a FEI Tecnai G20 at 200 kV. Ex-situ STEM imaging was performed at 200 kV on a probe corrected JEOL ARM 200, with a convergence angle of 27.5 mrad and a collection angle of 90-370 mrad. LC-TEM was done with a Hummingbird Scientific liquid flow holder. Images were analyzed with ImageJ, with some images subjected to a Gaussian blur to remove noise. Nanoparticle cross-sectional areas were measured by binarizing the images and summing black pixels in each nanoparticle.

Acknowledgements

This research was supported by the Interfacial Dynamics in Radioactive Environments and Materials (IDREAM), an Energy Frontier Research Center funded by the U.S. Department of Energy (DOE), Office of Science, Basic Energy Sciences (BES). PNNL is a multiprogram national laboratory operated for DOE by Battelle under Contract No. DE-AC05-76RL01830. A.W.R thanks the Royal Society for their support.

Reference

- (1) Chattot, R.; Asset, T.; Drnec, J.; Bordet, P.; Nelayah, J.; Dubau, L.; Maillard, F. Atomic-Scale Snapshots of the Formation and Growth of Hollow PtNi/C Nanocatalysts. *Nano Lett.* **2017**, *17* (4), 2447–2453.
- (2) Antolini, E.; Salgado, J. R. C.; Gonzalez, E. R. The Stability of Pt–M (M=first Row Transition Metal) Alloy Catalysts and Its Effect on the Activity in Low Temperature Fuel Cells. *J. Power Sources* **2006**, *160* (2), 957–968.
- (3) Wang, D.; Xin, H. L.; Hovden, R.; Wang, H.; Yu, Y.; Muller, D. A.; DiSalvo, F. J.; Abruña, H. D. Structurally Ordered Intermetallic Platinum-Cobalt Core-Shell Nanoparticles with Enhanced Activity and Stability as Oxygen Reduction Electrocatalysts. *Nat. Mater.* **2013**, *12* (1), 81–87.
- (4) Kim, H.; Robertson, A. W.; Kim, S. O.; Kim, J. M.; Warner, J. H. Resilient High Catalytic Performance of Platinum Nanocatalysts with Porous Graphene Envelope. *ACS Nano* **2015**, *9* (6), 5947–5957.
- (5) Liu, G.; Robertson, A. W.; Li, M. M.-J.; Kuo, W. C. H.; Darby, M. T.; Muhieddine, M. H.; Lin, Y.-C.; Suenaga, K.; Stamatakis, M.; Warner, J. H.; et al. MoS₂ Monolayer Catalyst Doped with Isolated Co Atoms for the Hydrodeoxygenation Reaction. *Nat. Chem.* **2017**, *9* (8), 810–816.
- (6) Tao, F. F.; Salmeron, M. In Situ Studies of Chemistry and Structure of Materials in Reactive Environments. *Science* (80-.). **2011**, *331* (6014), 171–174.
- (7) Evans, J. E.; Jungjohann, K. L.; Browning, N. D.; Arslan, I. Controlled Growth of Nanoparticles from Solution with In Situ Liquid Transmission Electron Microscopy. *Nano Lett.* **2011**, *11* (7), 2809–2813.

- (8) Sutter, E.; Jungjohann, K.; Bliznakov, S.; Courty, A.; Maisonhaute, E.; Tenney, S.; Sutter, P. In Situ Liquid-Cell Electron Microscopy of Silver–palladium Galvanic Replacement Reactions on Silver Nanoparticles. *Nat. Commun.* **2014**, *5*, 4946.
- (9) Zheng, H.; Smith, R. K.; Jun, Y.-W.; Kisielowski, C.; Dahmen, U.; Alivisatos, A. P. Observation of Single Colloidal Platinum Nanocrystal Growth Trajectories. *Science (80-.)*. **2009**, *324* (5932), 1309–1312.
- (10) Zhu, G.; Jiang, Y.; Lin, F.; Zhang, H.; Jin, C.; Yuan, J.; Yang, D.; Zhang, Z. In Situ Study of the Growth of Two-Dimensional Palladium Dendritic Nanostructures Using Liquid-Cell Electron Microscopy. *Chem. Commun.* **2014**, *50* (67), 9447.
- (11) Ross, F. M. *Liquid Cell Electron Microscopy*; Ross, F. M., Ed.; Cambridge University Press, 2016.
- (12) Woehl, T. J.; Jungjohann, K. L.; Evans, J. E.; Arslan, I.; Ristenpart, W. D.; Browning, N. D. Experimental Procedures to Mitigate Electron Beam Induced Artifacts during in Situ Fluid Imaging of Nanomaterials. *Ultramicroscopy* **2013**, *127*, 53–63.
- (13) Ross, F. M. Opportunities and Challenges in Liquid Cell Electron Microscopy. *Science (80-.)*. **2015**, *350* (6267), aaa9886-aaa9886.
- (14) Zheng, H.; Claridge, S. A.; Minor, A. M.; Alivisatos, A. P.; Dahmen, U. Nanocrystal Diffusion in a Liquid Thin Film Observed by in Situ Transmission Electron Microscopy. *Nano Lett.* **2009**, *9* (6), 2460–2465.
- (15) Verch, A.; Pfaff, M.; de Jonge, N. Exceptionally Slow Movement of Gold Nanoparticles at a Solid/Liquid Interface Investigated by Scanning Transmission Electron Microscopy. *Langmuir* **2015**, *31* (25), 6956–6964.
- (16) Chee, S. W.; Baraissov, Z.; Loh, N. D.; Matsudaira, P. T.; Mirsaidov, U. Desorption-Mediated Motion of Nanoparticles at the Liquid–Solid Interface. *J. Phys. Chem. C* **2016**, *120* (36), 20462–20470.
- (17) Park, J.; Elmlund, H.; Ercius, P.; Yuk, J. M.; Limmer, D. T.; Chen, Q.; Kim, K.; Han, S. H.; Weitz, D. A.; Zettl, A.; et al. 3D Structure of Individual Nanocrystals in Solution by Electron Microscopy. *Science (80-.)*. **2015**, *349* (6245), 290–295.
- (18) Joo, S.; Baldwin, D. F. Adhesion Mechanisms of Nanoparticle Silver to Substrate Materials: Identification. *Nanotechnology* **2010**, *21* (5), 55204.

- (19) Aissaoui, N.; Bergaoui, L.; Landoulsi, J.; Lambert, J.-F.; Boujday, S. Silane Layers on Silicon Surfaces: Mechanism of Interaction, Stability, and Influence on Protein Adsorption. *Langmuir* **2012**, *28* (1), 656–665.
- (20) Kasemo, B. Biological Surface Science. *Surf. Sci.* **2002**, *500* (1–3), 656–677.
- (21) Aureau, D.; Varin, Y.; Roodenko, K.; Seitz, O.; Pluchery, O.; Chabal, Y. J. Controlled Deposition of Gold Nanoparticles on Well-Defined Organic Monolayer Grafted on Silicon Surfaces. *J. Phys. Chem. C* **2010**, *114* (33), 14180–14186.
- (22) Zheng, J.; Zhu, Z.; Chen, H.; Liu, Z. Nanopatterned Assembling of Colloidal Gold Nanoparticles on Silicon. *Langmuir* **2000**, *16* (10), 4409–4412.
- (23) Ben Haddada, M.; Blanchard, J.; Casale, S.; Krafft, J.-M.; Vallée, A.; Méthivier, C.; Boujday, S. Optimizing the Immobilization of Gold Nanoparticles on Functionalized Silicon Surfaces: Amine- vs Thiol-Terminated Silane. *Gold Bull.* **2013**, *46* (4), 335–341.
- (24) To, T. D.; Nguyen, A. T.; Phan, K. N. T.; Truong, A. T. T.; Doan, T. C. D.; Dang, C. M. Modification of Silicon Nitride Surfaces with GOPES and APTES for Antibody Immobilization: Computational and Experimental Studies. *Adv. Nat. Sci. Nanosci. Nanotechnol.* **2015**, *6* (4), 45006.
- (25) White, E. R.; Mecklenburg, M.; Singer, S. B.; Aloni, S.; Regan, B. C. Imaging Nanobubbles in Water with Scanning Transmission Electron Microscopy. *Appl. Phys. Express* **2011**, *4* (5).
- (26) Zhu, G.; Jiang, Y.; Huang, W.; Zhang, H.; Lin, F.; Jin, C. Atomic Resolution Liquid-Cell Transmission Electron Microscopy Investigations of the Dynamics of Nanoparticles in Ultrathin Liquids. *Chem. Commun.* **2013**, *49* (93), 10944.
- (27) Craig, V. S. J. Very Small Bubbles at Surfaces—the Nanobubble Puzzle. *Soft Matter* **2011**, *7* (1), 40–48.
- (28) Egerton, R. F.; Li, P.; Malac, M. Radiation Damage in the TEM and SEM. *Micron* **2004**, *35* (6), 399–409.
- (29) Woehl, T. J.; Evans, J. E.; Arslan, I.; Ristenpart, W. D.; Browning, N. D. Direct in Situ Determination of the Mechanisms Controlling Nanoparticle Nucleation and Growth. *ACS Nano* **2012**, *6* (10), 8599–8610.
- (30) Woehl, T. J.; Prozorov, T. The Mechanisms for Nanoparticle Surface Diffusion and Chain Self-Assembly

Determined from Real-Time Nanoscale Kinetics in Liquid. *J. Phys. Chem. C* **2015**, *119* (36), 21261–21269.

- (31) Peterson, R. A.; Buck, E. C.; Chun, J.; Daniel, R. C.; Herting, D. L.; Ilton, E. S.; Lumetta, G. J.; Clark, S. B. Review of the Scientific Understanding of Radioactive Waste at the U.S. DOE Hanford Site. *Environ. Sci. Technol.* **2018**, *52* (2), 381–396.
- (32) Frens, G. Controlled Nucleation for the Regulation of the Particle Size in Monodisperse Gold Suspensions. *Nat. Phys. Sci.* **1973**, *241* (105), 20–22.
- (33) Jana, N. R.; Gearheart, L.; Murphy, C. J. Wet Chemical Synthesis of High Aspect Ratio Cylindrical Gold Nanorods. *J. Phys. Chem. B* **2001**, *105* (19), 4065–4067.